Word count: 7625

REVISION 2

The role of parent lithology in nanoscale clay-mineral transformations in a subtropical monsoonal climate

Lulu Zhao [a], Hanlie Hong [a,*], Ke Yin [a], Shi Cheng [a], Xinghong Wang [a], Thomas J. Algeo [a,b,c]

[a] *State Key Laboratory of Biogeology and Environmental Geology, Hubei Key Laboratory of Critical Zone Evolution, School of Earth Sciences, China University of Geosciences, Wuhan 430074, China*

[b] *Department of Geology, University of Cincinnati, Cincinnati, OH 45221-0013, USA*

[c] *State Key Laboratory of Geological Processes and Mineral Resources, China University of Geosciences, Wuhan 430074, China*

[*]Corresponding author: H. Hong (honghl8311@aliyun.com)

ABSTRACT

Clay minerals are among the most important reactive components of soil systems,

acting as a bridge linking organic and inorganic components. Lithology is a key factor in clay-mineral genesis and transformation, yet it has received scant attention to date at the nanoscale. Inferences regarding pedogenic clay-mineral transformations based on X-ray diffraction (XRD) are sometimes speculative, whereas mineralogic relationships documented by high-resolution transmission electron microscopy (HRTEM) are more robust due to direct evidence from lattice-fringe observations. In this contribution, the mineralogical and geochemical characteristics of four soils derived from different parent rock types (a gneiss, an Fe-rich siltstone, a sandstone, and a dolostone) from subtropical China were determined using HRTEM, XRD, and geochemical elemental data. The predominance of 2:1 clay minerals and kaolinite in the investigated soils is typical of subtropical climatic settings. Lattice-fringe sample images suggest the prevalence of topotactic transformations during clay-mineral alteration. Two distinct alteration pathways were observed in the investigated soils, one starting with chlorite and the other with illite, with convergence of mineralogic compositions towards kaolinite and crystalline iron and aluminum (oxyhydr)oxides. In the early stages of weathering, chlorite transformed into expandable clays through a continuous, solid-state mechanism with corrensite and/or randomly interstratified chlorite-vermiculite/chlorite-smectite as intermediate products. Unlike chlorite, which tends to form a 1:1 regularly interstratified phase, the weathering of illite commonly starts at layer edges. Under subtropical monsoonal climates, the precursor minerals in host rocks and aeolian materials determine the starting composition and, to a certain extent, the trajectory of clay-mineral transformation over time. With advanced

weathering, mineralogic convergence towards kaolinite and Fe/Al-(oxyhydr)oxides tends to obscure the initial substrate composition. This study advances our understanding of the role of parent lithology in clay-mineral evolution at the nanoscale.

Keywords: pedogenesis; chemical weathering; HRTEM; smectite; chlorite; corrensite

INTRODUCTION

Clay minerals represent an important component of the near-surface crustal environment of Earth and Mars (Hazen et al. 2013; Schroeder 2018). In the surficial weathering zones, primary minerals may transform into other clay species through a sequence of intermediate phases prior to the formation of endmember products (Churchman and Lowe 2012; He et al. 2017; Weil and Brady 2017). Clay minerals are naturally abundant in temperate and subtropical climates, and 2:1 clay minerals are oftentimes enriched in nutrients essential for plant growth (e.g., potassium and magnesium) (Velde and Meunier 2008; Cuadros 2017; Churchman 2018; Bakker et al. 2019). Clay minerals also play a key role in the preservation of natural organic carbon and influence global carbon cycling (Hemingway et al. 2019; Kleber et al. 2021). Unraveling the mechanisms and driving forces of clay-mineral neoformation and transformation is of vital importance for understanding the evolution of geological and pedogenic environments and mineral-environment interactions through time (Wilson

64 2004; Ryan and Huertas 2009; Cuadros 2017).

65 Neoformation and transformation of clay minerals are strongly dependent on the
66 lithology of parent materials (Churchman and Lowe 2012; Yousefifard et al. 2015;
67 Watanabe et al. 2017; Egli and Mirabella 2021). Yousefifard et al. (2015) investigated
68 soils developed on various plutonic rocks and found variation in soil physicochemical
69 properties but no significant differences in clay mineralogy, which was attributed to
70 their similar arid/semiarid climate background. Watanabe et al. (2017) investigated
71 the B horizons of soils developed under a humid tropical climate from various parent
72 materials (i.e., felsic, intermediate and mafic igneous as well as sedimentary rocks)
73 and found that parent lithology plays an important role in controlling
74 secondary-mineral distributions. However, the influence of soil parent materials on the
75 formation and transformation of clay minerals under a subtropical climate has been
76 insufficiently investigated to date. In particular, to the best of our knowledge, an
77 assessment of such influences has never been undertaken at the nanoscale.

78 Accurate and detailed characterization of the mixed-layer clay phases (i.e.,
79 interstratified clay phases) is key to clay-mineral alteration investigations. X-ray
80 diffraction (XRD) is the most widely used tool for characterizing interstratified clay
81 minerals, but it provides information averaged from millions of crystals rather than
82 from individual crystals (Wang et al. 2019). For this reason, XRD analysis may miss
83 critical information on mineral weathering pathways, especially when mineral
84 abundances are low. As an alternative, high-resolution transmission electron
85 microscopy (HRTEM) enables direct imaging of clay minerals at the nanoscale (e.g.,

Kogure and Inoue 2005; Liu et al. 2019; Kogure 2020). A combination of XRD and HRTEM represents the most powerful approach for characterizing clay minerals, especially transformations between different clay minerals (Kogure et al. 2013). However, HRTEM investigations of parent-rock influences on pedogenic clay-mineral alteration are still rare.

In order to advance our understanding of the relationship of clay-mineral transformations to parent lithology at a nanodomain scale, we investigated soils developed on various parent rocks (i.e., gneiss, siltstone, sandstone, and dolostone) under a subtropical monsoonal climate. We performed detailed mineralogical and geochemical investigations relying on nanoscale observations by HRTEM. We did not investigate the entire soil profile in detail as done in most conventional pedological studies. Rather, we focused on the B horizon of each soil profile, i.e., the zone of illuviation and translocation, which contains less organic matter compared with the overlying O and A horizons but greater abundances of clays and iron oxides washed down from the horizons above (Weil and Brady 2017). By highlighting the fate of illite and chlorite and their transformative pathways to interstratified clay minerals during pedogenic alteration of various parent rock types under similar climatic conditions, the results of this study have the potential to improve our understanding of controls on clay-mineral assemblages on Earth as well as on Mars.

MATERIALS AND METHODS

Climatic/geological background and sampling

The Zigui study area (~110°40'-111°00'N, ~30°50'-31°00'E) is located near Yichang City, Hubei Province, central China (Fig. 1). The area is bifurcated by the northward-flowing Yangtze River, with a general decrease in elevation from southwest to northeast. This region has a subtropical monsoonal climate characterized by highly seasonal/monsoonal variations in temperature and precipitation, with warm humid summers and cool dry winters. Mean annual temperature is 13.8 °C (1.5 °C in winter and 24.5 °C in summer), and mean annual precipitation is ~1580 mm (Hersbach et al. 2019). Subtropical deciduous thickets and dwarf forests represent the dominant vegetation biomes. The Zigui area in the Middle Yangtze region contains highly variable rock types (strata ranging in age from Silurian to Quaternary) that crop out in relatively close geographic proximity (i.e., within a 20-km radius) (Hubei Province Geological Survey 1965). Jurassic sandstone, Triassic limestone, and Cambrian dolostone are widely distributed in the study area, especially along the Yangtze River. Few faults appear in the study area, and the principal structure is the Zigui Syncline (Hu et al. 2021). The study area has soils of diverse appearance including yellowish-brown, purple, and calcareous soils that are classified as Alfisols or Inceptisols in the USDA soil taxonomy (Table S1; Shi et al. 2004; Soil Survey Staff 2014). For the present study, soil samples were collected from a siltstone-derived purple (5P 3/2; note that all color descriptors refer to the Munsell color chart) soil at Gejiabei (GJB), a gneiss-derived reddish-brown (2.5YR 4/4) soil at Zhongbazi (ZBZ),

a sandstone-derived yellowish-brown (10YR 5/4) soil at Jiuqunao (JQN), and a dolostone-derived brownish yellow (10YR6/8) calcareous soil at Taishangping (TSP) (Table S1).

X-ray diffraction (XRD)

Each sample was air-dried and ground to pass through a <74-μm (200-mesh) sieve prior to mineralogical and geochemical laboratory procedures. Both bulk and clay-fraction samples were analyzed by X-ray diffraction (XRD). Prior to XRD analysis, organic carbon was removed from an aliquot of each sample using a 30 % H_2O_2 solution. Unoriented bulk powders were analyzed using a back-loaded procedure. The clay fraction (<2 μm) was isolated from suspension by centrifugation after dispersion. Oriented clay-fraction mounts were generated by pipetting slurries of the suspensions onto glass slides and drying them at room temperature. These oriented slides were subjected to various diagnostic treatments to facilitate clay-mineral identification (Moore and Reynolds 1989): air-dried XRD mounts (AD), ethylene glycol solvation (EG), K-saturation at room temperature (K25), and K-saturation with heating to 350 °C (K350) and 550 °C (K550) for 2h. The K saturation procedure was performed on recycled powders that were recovered from the AD mounts by scraping. Both bulk and clay-fraction samples were irradiated over the range 3°-65° 2θ at a scanning speed of 4° 2θ per minute and a resolution of 0.02° 2θ. The XRD patterns were obtained using a Panalytical X'pert PRODY2198 diffractometer (Netherlands) with a Cu Kα radiation source (40 kV, 40 mA). The Jade software was used to fit

experimental XRD pattern of *00l* reflections over the 3.5-15° 2θ range. The Voigt function was applied to fit the peaks of the EG spectra. Prior to peak fitting, the background of each XRD pattern was subtracted based on a cubic spline method with an automated threshold of 5 sigma using the Jade software. Various combinations of peaks were tested to find the one yielding the minimum residual signal.

High-resolution transmission electron microscopy (HRTEM)

Clay-mineral weathering and transformations were observed at the nanoscale by HRTEM on ion-milled sections through the study samples. HRTEM images were taken with a JEOL 2010 high-resolution transmission electron microscope (Japan) equipped with an energy-dispersive X-ray (EDX) spectrometer. The HRTEM analysis was performed at an accelerating voltage of 200 kV with a nominal point resolution of ~2 Å. Clay-fraction specimens were air-dried at room temperature, then embedded with epoxy resin between two glass slides to obtain highly oriented clay particles. After hardening, the glass slides were cut using a diamond wheel to laths of ~1 mm thickness. The laths were thinned to ~50 μm by mechanical grinding and then argon-ion milled to a final thickness of ~100 nm. Selected areas of TEM images were digitized and processed to remove noise and areas of amorphous material using a Wiener filter developed by K. Ishizuka and implemented with Gatan Digital Micrograph software (Kogure et al. 2013).

171 **Soil geochemical and physiochemical analyses**

172 Major-element concentrations were determined by X-ray fluorescence (XRF)
173 analysis using a Shimadzu XRF-1800 sequential spectrometer (Japan). Sample
174 powders were fused into glass beads using a $Li_2B_4O_7$:$LiBO_2$ (6:11) compound flux to
175 which a small amount of LiBr was added. Loss-on-ignition (LOI) values were
176 determined after heating the samples at 1050 °C for 1 h. Analytical uncertainties are
177 better than ± 1.0 wt. %. Trace element and rare-earth element (REE) concentrations
178 were measured using an Agilent 7500a inductively coupled plasma mass spectrometer
179 (ICP-MS), with an analytical precision of < 4% for REEs and 4–10% for other trace
180 elements. Ce and Eu anomalies (i.e., Ce/Ce* and Eu/Eu*) were calculated using the
181 following equations (Compton et al. 2003):

182

183 $$\frac{Ce}{Ce*} = \frac{(Ce_{soil}/Ce_{UCC})}{[(La_{soil}/La_{UCC})^{0.5}(Pr_{soil}/Pr_{UCC})^{0.5}]} \quad (1)$$

184 $$\frac{Eu}{Eu*} = \frac{(Eu_{soil}/Eu_{UCC})}{[(Sm_{soil}/Sm_{UCC})^{0.5}(Gd_{soil}/Gd_{UCC})^{0.5}]} \quad (2)$$

185

186 where the subscripts “soil” and “UCC” represent the REE concentrations in the bulk
187 soil sample and upper continental crust (UCC) (McLennan 2001), respectively. Values
188 <1 and >1 represent negative and positive Ce and Eu anomalies, respectively.

189 Soil acidity (pH) and redox potential (Eh) were measured on air-dried samples (<2

mm) from a soil:deionized water solution in a 1:2.5 ratio using a pH/Eh electrode (ORP-501, INESA, China).

RESULTS

Pedon descriptions and general soil properties

The main physical and chemical properties of the four soil pedons (GJB, ZBZ, JQN, and TSP) are shown in Tables S1 and S2. The B horizons of the four soils are slightly acidic to near neutral, with pH values ranging from 6.3 to 7.2. The GJB soil was developed on purple siltstones intercalated between green siltstones of Jurassic age. The A, B, and C horizons have a friable consistency and a subangular blocky structure, with grain size increasing from the A to the C horizon. The ZBZ soil was developed on a gneissic parent rock of Proterozoic age. It has an obvious O horizon and is the thickest of the four soils. JQN soil was developed on a feldspathic quartz sandstone of Cambrian age, and has the lowest pH (6.1-6.4) of the four soils. The TSP soil developed on a dolostone host rock of Cambrian age and is therefore calcareous. The boundary between the weathered layer and the underlying parent rock is abrupt and may represent a lithological discontinuity.

XRD analysis

XRD analysis of randomly oriented mounts wasused to identify the bulk-mineral

compositions (mainly non-clay-mineral phases) of the study samples (Fig. 2a). Feldspars, quartz, mica, clay minerals including interstratified clay minerals, and hematite were identified in the bulk-sample XRD patterns. Hornblende is found only in the gneiss-derived ZBZ soil, as indicated by peaks at 8.4, 3.1 and 2.7 Å, and dolomite (2.9 Å) is found only in the dolostone-derived soil (Fig. 2a). The XRD patterns of the oriented mounts show the presence of goethite and gibbsite (Fig. 3). In these spectra, the (060) region can reveal the presence of trioctahedral and dioctahedral phases (Fig. 2b). A predominance of dioctahedral (~1.50 Å) over trioctahedral (~1.53 Å) components is evident in the investigated soils (Fig. 2b).

The XRD patterns of the oriented mounts show notable differences in clay-mineral assemblages among the soil samples derived from different parent rocks (Fig. 3). At GJB, the AD treatment yielded distinct peaks at 14.4, 12.7, 10.1 and 7.1 Å, but in the K550 treatment, the peak at 7.1 Å disappeared while the 14.3-Å peak remained, suggesting the presence of chlorite. A significant portion of the ~14.3-Å peak shifted to 15-18 Å after EG treatment and collapsed to ~10 Å after K25 treatment, indicating the presence of both smectite and vermiculite layers, either as discrete clay minerals or in interstratified clay minerals such as interstratified chlorite-vermiculite (C-V) or chlorite-smectite (C-S) (Fig. 3a), and the potential occurrence of C-V (or C-S) was further confirmed by HRTEM observations. The peak at ~12 Å became more prominent in the K350 and K550 treatments compared to the K25 treatment, suggesting the presence of hydroxy-interlayered minerals (HIM). The peak at 12.3 Å split into two peaks after EG treatment, at ~9.4 Å and ~13.7 Å,

potentially suggesting the presence of interstratified illite-smectite (I-S). The peak at ~25.3 Å may correspond to corrensite (Drits et al. 2011), although this mineralogic identification must be further confirmed by HRTEM observation (see *HRTEM analysis* section).

The main differences in oriented XRD patterns between the gneiss-derived ZBZ and the siltstone-derived GJB include the near-absence of peaks in the region of ~10-15 Å for the K350 and K550 treatments (Fig. 3a, b). Thus, XRD analysis shows that the ZBZ soil contains little chlorite and interstratified C-V (or C-S) but measurable kaolinite (Fig. 3a, b). A peak at 14.6 Å in the AD and K25 treatments shifted to ~10.1 Å in the K350 treatment, possibly indicating the presence of HIM with a relatively low degree of Al-polymerization (Moore and Reynolds 1989; Korchagin et al. 2019). At JQN, the situation is similar to that of the GJB soil (Fig. 3a, c). The main differences include the absence of chlorite and occurrence of interstratified kaolinite-smectite (K-S) at JQN. At TSP, no smectite was observed, and expandable clay minerals may consist of vermiculite based on expansion of (001) to ~15.8 Å rather than to >16.6 Å, as for smectite. A portion of the peak at 14.3 Å collapsed to ~10 Å after K25 treatment, further confirming the occurrence of vermiculite. The presence of a residual peak at 14.3 Å in the K25 treatment, which collapsed to ~12.6 Å in the K350 and to ~11 Å in the K550 treatments, indicates the presence of HIM. Illite and kaolinite can also be identified in the TSP soil, but chlorite is absent (Fig. 3d). Figure 3e shows the peak deconvolution of the four EG patterns. Clay-mineral assemblages indicated in Fig. 3e were determined from mineral identifications on the basis of Fig.

254 3a-d, and thus these two types of XRD patterns show consistent clay-mineral
255 assemblages.

256

257 **HRTEM analysis**

258 Differences in the clay-mineral assemblages among the four study soils were
259 discussed in the *XRD analysis* section. Below, we focus on nanoscale weathering of
260 the two main "primary" clay minerals (chlorite and illite) in the study soils.
261 Representative lattice-fringe images showing clay-mineral transformations for each
262 soil are presented in Figures 4-7.

263

264 *Weathering of chlorite*

265 In the siltstone-derived GJB soil, the *d*-spacings of clay minerals vary from 7
266 to >20 Å (Fig. 4). Consistent with the XRD results, HRTEM images reveal the
267 presence of corrensite, a weathering product of chlorite that has a trioctahedral 2:1
268 structure with 1:1 ordered interstratifications of chlorite and smectite (C-S) or chlorite
269 and vermiculite (C-V) (Fig. 4a-c). Corrensite is identified as 1:1 ordered
270 interstratifications of chlorite and smectite (or vermiculite) with evident brucite-like
271 hydroxide sheets (hereafter called "B sheet") and lattice-fringe spacing of 24-26 Å
272 (Fig. 4a-b; Kogure et al. 2013). The B sheet in corrensite and chlorite can be
273 unambiguously identified as bold dark lines, as indicated by arrows labeled "B" in
274 Figure 4a-b. The EDX spectra show that the corrensite zones contain amounts of Si,

Al, Fe and Mg (Fig. 4g, i) generally consistent with the chemical compositions of corrensite and its alteration products.

Further transformation of corrensite to interstratified 14-/10-Å layers in the GJB soil is seen in HRTEM images (Fig. 4a-b). Combined with the XRD data, we interpret the interstratified 14-/10-Å layers to be partially collapsed from interstratified C-V (or C-S) (similar to the case observed by Aspandiar and Eggleton 2002), as vermiculite or smectite layers in corrensite may be sensitive to the high-energy electron beam during TEM observation. The collapsed layers with a thickness of ~10 Å can occur either at the edge of or within corrensite particles (Fig. 4a-b). The transformation of the ~24-Å corrensite to 1:1 randomly interstratified C-V or C-S (i.e., the interstratified C-V or C-S that is 1:1 ordered) is shown at the upper right of Figure 4b. The dominant fringes in Figure 4c may also correspond to corrensite-derived randomly interstratified C-V (or C-S), with lattice fringes of both ~10 Å and ~12 Å corresponding to vermiculite or smectite layers in the interstratified clay minerals. Figure 5a shows a highly weathered, Fe-/Mg-containing chlorite particle in the ZBZ soil, in which partially collapsed vermiculite (or smectite) layers, corrensite consisting of 25-Å layers, and a few unaltered chlorite layers can be observed. The magnified image in Figure 5a shows adjacent packets of chlorite and corrensite, possibly suggesting the weathering of chlorite into corrensite.

Similarly, the 10- and 7-Å layers are randomly distributed in the 14-Å packets in the JQN soil, which may indicate the transformation of chlorite to randomly interstratified C-V or C-S (or discrete vermiculite and smectite) and then possibly to

297 kaolinite (Fig. 6a; Aspandiar and Eggleton 2002). The transformation of chlorite to
298 corrensite has not been found in the JQN soil. The EDX spectrum shows that the
299 interstratified clay minerals in Figure 6a contain Fe, Mg, and Ca (Fig. 6e), suggesting
300 that the observed fringes are more likely randomly interstratified C-S.

301

302 *Weathering of illite*

303 A succession of 10-Å layers in the GJB soil can be seen in Figure 4d-e. The
304 straight 10-Å fringes with few defects are characterized by relatively low Fe and Mg
305 contents and a certain amount of K (Fig. 4i-j), indicative of illite. The enlarged image
306 in Figure 4d shows filtered periodic 22-Å layers in contact with 12-Å packets on an
307 illite substrate (domain). The periodic 22-Å layers may correspond to interstratified
308 illite-smectite (I-S) or illite-vermiculite (I-V), and the periodic 12-Å layers to partially
309 collapsed smectite or vermiculite (Aspandiar and Eggleton 2002). These relationships
310 may represent the mineral weathering sequence of illite to I-S or I-V and then to
311 smectite or vermiculite.

312 A clay particle containing K in the ZBZ soil in Figure 5b shows a curved
313 morphology, in which co-occurrence of 10- and 11-12-Å fringes may indicate the
314 weathering transformation of illite to vermiculite (or smectite). In the JQN soil,
315 straight lattice fringes with 10-Å spacing contain less Mg and Fe and more K
316 (compared to weathered chlorite), which is indictive of illite layers (Fig. 6b, f). In
317 Figure 6b, the common layer packets are composed predominantly of 11- to 13-Å

318 layers, which may correspond to either smectite or vermiculite. This spatial
319 arrangement suggests that the smectite or vermiculite layers formed through
320 weathering of illite. Weathering of illite is common in the TSP soil (Fig. 7). The edges
321 of illite were altered to layers with spacings of 11 to 12 Å, indicative of expandable
322 clay minerals (Fig. 7). Some 7-Å layers are found near the 10- and 11-13-Å fringes,
323 suggesting transformation of smectite (or vermiculite) to kaolinite or mixed-layer
324 kaolinite/smectite during late-stage weathering (Fig. 7).

325

326 *Occurrence of Fe/Al-(hydr)oxides*

327 In GJB, cross-lattice fringes with thicknesses of ~3.7 Å and ~4.8 Å are
328 sometimes found along the 10-11-Å lattice fringes (Fig. 4f), possibly indicating a
329 close spatial relationship among hematite (~3.7 Å), gibbsite (~4.8 Å) and smectite (or
330 vermiculite). In JQN, Fe-(hydr)oxides with spacings of 3.7 Å and 4.2 Å, indicative of
331 hematite and goethite, are found along clay minerals with fringe layer spacings of 12
332 Å and 7 Å (Fig. 6c).

333

334 **Geochemical compositions**

335 The results of elemental analyses of the four study soils and their parent rocks
336 are presented in Table S3. All four soils have relatively high SiO_2 (61.2–72.4 %) and
337 Al_2O_3 (12.7–17.6 %) contents. The amounts of alkali and alkaline earth elements,
338 such as MgO, CaO, K_2O, and Na_2O, do not exceed 5 % in most cases. Compared to

339 the other soils, the dolostone-derived TSP soil has the highest concentration of Mg
340 (2.6 %) and the lowest concentration of Na (0.5 %). In contrast, the JQN soil, which
341 developed from feldspathic quartz sandstone, has the highest concentration of Na_2O
342 (4.1 %; probably sourced from albite) and the lowest concentration of MgO (1.4 %).
343 The ZBZ soil, which developed from gneiss, has the highest concentration of CaO
344 (5.3 %; probably sourced from hornblende) and the lowest concentration of K_2O
345 (0.4 %). The GJB soil, which developed from siltstone, has the highest Fe_2O_3 (7.6 %;
346 sourced from chlorite, biotite, and Fe-(hydr)oxides) and K_2O concentrations (3.4 %,
347 sourced from mica group minerals) and the lowest CaO concentration (0.8 %).

348 Total REE contents vary from ~60 to ~200 ppm for the four study soils, which
349 mostly show modest enrichment relative to the parent rocks. Specifically, the total REE
350 concentration (ΣREE) of the TSP soil (205 ppm) is about four times higher than its
351 parent rock (53 ppm). In contrast, the soils of GJB, ZBZ, and JQN have relatively lower
352 REE concentrations, with ΣREE values only 1–1.3 times higher compared to their
353 parent rocks. For the GJB, ZBZ, and TSP soils, the LREE/HREE ratio ranges from 8.5
354 to 9.9, indicating a significant fractionation between LREE and HREE. The TSP soil
355 has a similar geochemical composition to nearby Quaternary red soils, with elemental
356 changes of less than a factor of two except for Ca and Mg (Fig. S1). All study samples
357 show slightly negative Ce anomalies with a mean Ce/Ce* of 0.93. Eu is mildly enriched
358 in the study soils (Eu/Eu* > 1.1 for ZBZ, GJB, and JQN) except for TSP (Eu/Eu* =
359 0.94). Positive Eu anomalies may be related to the presence of albite and K-feldspar
360 in the parent rock, which tend to be Eu-enriched (Vázquez-Ortega et al. 2015).

DISCUSSION

Solid-state transformations among pedogenic clay minerals

As suggested by XRD results, the predominance of 2:1 clay minerals (smectite, vermiculite, illite, and their associated assemblage of mixed-layered minerals) and kaolinite is typical of soils generated under subtropical climate conditions. HRTEM analysis can provide additional insights into pedogenic clay-mineral transformations beyond XRD analysis. For example, XRD analysis of oriented clay-fraction mounts did not detect the presence of chlorite layers in the ZBZ and JQN soils, probably because chlorite is present at low concentrations, its pattern overlaps with those of other ~14-Å clay minerals, and chlorite particles in these soils are often highly weathered. XRD can identify the overall clay-assemblage composition of soils, but it may miss important information regarding the formation and transformation of clay minerals during pedogenic weathering. Inferences regarding pedogenic clay-mineral transformations based on XRD are sometimes speculative, whereas mineralogic relationships documented by HRTEM are more robust due to direct evidence from lattice-fringe observations at the nanoscale.

Interstratification among clay minerals as well as co-occurrence of interstratified clay minerals and endmember (i.e., non-interstratified) clay minerals, as commonly observed by lattice-fringe HRTEM imaging, document the prevalence of solid-state topotactic exchanges during the transformation from one clay mineral into another as

382 weathering advances without complete dissolution and re-precipitation. Topotactic
383 exchange in clay minerals, which is common in supergene weathering environments,
384 can lead to the progressive transformation of chlorite or illite into expandable 2:1 clay
385 minerals as well as smectite/vermiculite group minerals and thence into kaolinite via
386 mixed-layer intermediates (e.g., Wilson 2004; Hong et al. 2012, 2014; Andrade et al.
387 2019, 2020; Fang et al. 2019).

388 The main pathways for clay-mineral formation and transformation in soils derived
389 from the four parent rocks of this study are summarized in Figure 8. Topotactic
390 alteration from chlorite to 2:1 clay minerals proceeds via the disruption of the
391 interlayer brucite-like sheet (hydroxide sheet in Fig. 8), releasing Mg, Fe, and small
392 amounts of Al (Aspandiar and Eggleton 2002; Kogure et al. 2013). Mg goes into
393 solution and Fe and Al precipitate as Fe- and Al-(oxyhydr)oxides (Figs. 4f and 6c).
394 This process usually involves initial generation of corrensite and/or randomly
395 interstratified C-V or C-S phases (Figs. 4-6; Banfield and Murakami 1998; Aspandiar
396 and Eggleton 2002; Sugimori et al. 2008). Corrensite is defined as a regular 1:1
397 interstratification of chlorite and either vermiculite or smectite (i.e., regular
398 interstratification of C-V/C-S) (Brigatti and Poppi 1984). The typical corrensite unit
399 (two 2:1 layers and a brucite-like sheet between them) has basal heights of 24-28 Å in
400 TEM photos (Kogure et al. 2013). Chlorite is transformed to expandable 2:1 clay
401 phases through a continuous, solid-state exchange mechanism with corrensite and/or
402 randomly interstratified C-V/C-S as intermediate products (Figs. 4 and 5). Corrensite
403 has a strong tendency to form in the initial stage of weathering, and appears to be a

404 mineral of relative stability and frequent occurrence (e.g., Aspandiar and Eggleton
405 2002; Sugimori et al. 2008; Kogure et al. 2013). The loss of Mg from the interlayer
406 brucite-like sheet between a pair of 2:1 layers increases the Mg-O bond in the
407 alternating brucite-like sheets, leading to regular interstratification during the earliest
408 stages of chlorite weathering (Norrish 1973; Aspandiar and Eggleton 2002).
409 Alteration from corrensite to randomly interstratified C-V or C-S may occur in the
410 next weathering stage, when more vermiculite-like layers are present in the
411 corrensite-like packets (Fig. 4a-c).

412 Illite was also found to transform by a solid-state topotactic mechanism to
413 pseudomorphs of oriented expandable 2:1 clay minerals through loss of potassium
414 from interlayer sites (Figs. 4-7; Wilson 1999). Illite-group minerals tend to develop
415 frayed edges on the margins of the interlayer site through weathering (Nakao et al.
416 2017). Unlike chlorite, which tends to form a 1:1 regularly interstratified phase, the
417 weathering of illite commonly starts at the edges (Figs. 4-7). In the next weathering
418 stage, neoformed expandable 2:1 clays are transformed into kaolinite via mixed-layer
419 intermediates (e.g., K-S). This transformation proceeds via stripping of Si tetrahedra
420 and the solid-state replacement of octahedral Mg or Fe by Al at the atomic level,
421 without complete lattice disruption (Ryan and Huertas 2009; Andrade et al. 2019).
422 These topotactic alterations release a series of base cations, with loss of Mg, Ca, and
423 K from the soil system via leaching, whereas Fe and Al are commonly retained via
424 formation of Fe/Al (oxyhydr)oxides such as hematite, goethite, and gibbsite (Figs. 3,
425 4f and 6c).

426

427 **Effect of lithologic variation on clay-mineral evolution pathway**

428 The four study soils exhibit pronounced differences in major-element chemistry
429 and mineralogical characteristics (Fig. 2 and Table S3). The siltstone-derived GJB soil
430 was characterized by relatively high Fe and K concentrations, while the
431 gneiss-derived ZBZ soil had high Ca, sandstone-derived JQN soil had high Na, and
432 the dolostone-derived TSP soil had high Mg concentration. Their mineralogical
433 characteristics are generally consistent with these geochemical differences. The GJB
434 soil was characterized by relatively high chlorite (and mica) contents, while the ZBZ
435 soil had high hornblende, JQN soil had high albite, and the TSP soil had high
436 dolomite content. These differences determine heterogeneities in clay-mineral
437 assemblages during weathering and diagenetic transformation.

438 HRTEM images reveal the following weathering sequence for chlorite in a
439 subtropical monsoonal climate: chlorite → corrensite or randomly interstratified
440 C-V/C-S → smectite or vermiculite → kaolinite and Fe/Al (oxyhydr)oxides (Fig. 8).
441 Discrete chlorite particles in a soil are commonly inherited from the parent rocks or
442 originate from early alteration of Fe- and Mg-bearing primary minerals such as
443 hornblende (Churchman and Lowe 2012). Among the study soils, HRTEM provides
444 evidence of the transformation of chlorite to corrensite only in the siltstone-derived
445 GJB and the gneiss-derived ZBZ soils. HRTEM also reveals that chlorite transforms
446 to expandable 2:1 clay phases (vermiculite or smectite) with corrensite and/or

447 randomly interstratified C-V/C-S as intermediate products (Figs. 4 and 5). As parent
448 materials for the formation of corrensite, the GJB and ZBZ soils contain Fe/Mg-rich
449 minerals such as chlorite and hornblende, which can readily weather into chlorite
450 (Figs. 2 and 3). Corrensite, which is a common early-stage weathering product, can
451 form via weathering of chlorite, yielding randomly interstratified chlorite-corrensite
452 or corrensite-vermiculite (Banfield and Murakami 1998; Aspandiar and Eggleton
453 2002).

454 Unlike in the GJB and ZBZ soils, 1:1 regular interstratification of chlorite-like
455 and vermiculite-like packets (i.e., corrensite) was not observed in the
456 sandstone-derived JQN soil (Fig. 6). In general, formation of corrensite through
457 weathering is common in environments with limited solution access and restricted
458 flushing but rare in well-drained soil profiles (Aspandiar and Eggleton 2002). We infer
459 that the absence of corrensite in the sandstone-derived JQN soil is related to its
460 well-drained environment, itself the product of the relatively large pore and particle
461 sizes of the soil. In addition, the JQN parent rock contains few Mg- and Fe-bearing
462 minerals, and, thus, the soil has low contents of Mg and Fe, retarding formation of
463 corrensite.

464 Smectite is absent in the calcareous soil (TSP) but is present in the other three soils
465 (Fig. 3). The parent rocks of GJB, ZBZ, and JQN contain a suite of pre-existing
466 minerals that weather to provide a broad mix of secondary mineral products and
467 cations. Carbonate parent rocks, however, release Ca (and Mg) and H_2CO_3 instead of
468 producing silicate minerals when they react with water. Clay minerals in the TSP

469 soil are mainly derived from inheritance and/or weathering of eolian materials.
470 Similar geochemical (especially REE) distributions between the TSP soil and
471 Quaternary red soils in Hubei Province suggest that eolian materials in the former may
472 have been derived from the latter (Table S3; Fig. S2). Chlorite is present either as a
473 discrete mineral phase or as interstratifications in mixed-layer clay minerals (Figs. 4-6)
474 in all soils except for the dolostone-derived TSP soil. Quaternary red soils contain
475 little chlorite, which can explain the absence of chlorite and associated clay minerals in
476 the TSP soil. The origin of smectite is traced back to both chlorite and trioctahedral
477 mica (i.e., biotite), and neoformation of smectite is retarded if the parent mica has a
478 predominantly dioctahedral structure (Righi et al. 1999; Egli and Mirabella 2021).
479 Indeed, neoformation of smectite often requires a minimal amount of chlorite or
480 trioctahedral mica (Egli et al. 2001, 2003; Egli and Mirabella 2021). In addition, the
481 Mg provided by weathering of dolomite favored formation of vermiculite rather than
482 smectite in the TSP soil. In the other three soils, prevailing acidic conditions are
483 unfavorable for neogenesis of smectite but favorable for solid-state transformation of
484 precursor phases to smectite via acid leaching. HRTEM images also support the
485 inference that smectite was derived from progressive smectization of illite and/or
486 chlorite (Figs. 4-7). Transformation of illite to smectite is evident in the ZBZ soil (Fig.
487 5), which can be attributed to its Ca-enriched/K-depleted condition.

488 In summary, parent lithology determines the starting point and, to a certain extent,
489 the trajectory of clay-mineral transformations over time. Two discrete alteration
490 pathways were observed in the investigated soils, one starting with chlorite (or

hornblende and trioctahedral mica, precursors of chlorite) and the other starting with illite (or mica and feldspar, precursors of illite), with a mineralogic convergence towards kaolinite and Fe/Al-(oxyhydr)oxides as weathering proceeds (Fig. 8b). The influence of rock type is most prominent in the early stages of weathering, whereas climatic conditions gradually become more important in the neoformation and transformation of clay minerals as weathering intensifies. The study area has a typical subtropical monsoonal climate with annual wet and dry cycles. The contents of alkali and silica in the soil diminish with increasing rainfall and seasonally saturated conditions. The climatic conditions of southern China induce high rates of elemental loss and promote transformation of intermediate 2:1 clay minerals into 1:1 clay phases (Hong et al. 2012, 2015; Li et al. 2020). Under contrasting subtropical climate conditions, kaolinite and hydrous aluminum and iron oxides become predominant during late-stage weathering (Velde and Meunier 2008; Churchman and Lowe 2012). Again, climatic influences gradually override lithologic influences on clay mineral alteration during late-stage weathering, and kaolinite and Fe/Al-(oxyhydr)oxides become predominant in the soil regardless of parent-rock type.

IMPLICATIONS

Clay minerals represent the most abundant natural reactive solids in the Earth's Critical Zone (Schroeder 2018). Advancing our knowledge of chemical weathering and neoformation and transformation of clay minerals in the Earth's surface is

512 essential for a better understanding of the role of clay minerals in surficial processes.
513 The present study demonstrates that HRTEM offers distinct advantages over XRD and
514 spectroscopic analyses in investigations of clay-mineral transformations and
515 pedogenic weathering, as it can provide detailed and direct evidence of clay
516 transformations at a nanodomain scale. Our findings show that parent lithology can
517 exert a strong influence on pedogenic weathering at both soil-profile and atomic
518 scales. Furthermore, the insights gleaned at an atomic scale may be distinct from
519 those generated at a larger scale. Under uniform climatic conditions such as in a
520 subtropical monsoonal zone, clay-mineral assemblages can be highly heterogenous at
521 both the soil-profile scale and the nanoscale, which is attributable to heterogeneity in
522 parent-rock types. On Mars, clay minerals are highly complex and heterogeneous and
523 preserve a record of water-rock interactions, the formation and alteration of which are
524 considered to have been controlled by soil-forming factors such as climate and parent
525 materials (Ehlmann et al. 2009). However, Martian mineralogy has been investigated
526 to date only using XRD and spectroscopic techniques, which are unable to unravel
527 specific mineral transformations at a nanoscale. We recommend application of
528 HRTEM analysis of clay-bearing samples returned from Mars in the future, and in
529 clay-bearing martian meteorites, to improve knowledge of the neoformation and
530 transformation of clay minerals on Mars.

531

ACKNOWLEDGMENTS

We are grateful to Pengtao Yang, Li Chen, Qian Fang, Chen Liu, and Yanlong Dong for field and laboratory assistance. We also thank the editor Dr. Lindsay J McHenry and the anonymous reviewers for their suggestions and constructive comments that substantially improved the manuscript. This work was supported by National Natural Science Foundation of China (42002042, 41972040, 42172045, and 42102031), China Postdoctoral Science Foundation (2020M672440), and Fundamental Research Funds for the Central Universities, China University of Geosciences (Wuhan) (No. CUG170106).

REFERENCES CITED

Andrade, G.R.P., Azevedo, A.C.D., Lepchak, J.K., and Assis, T.C. (2019) Weathering of Permian sedimentary rocks and soil clay minerals transformations under subtropical climate, southern Brazil (Paraná State). Geoderma, 336, 31-48.

Andrade, G.R.P., Furquim, S.A.C., Nascimento, T.T.V.D., Brito, A.C., Camargo, G.R., and Souza, G.C.D. (2020) Transformation of clay minerals in salt-affected soils, Pantanal wetland, Brazil. Geoderma, 371, 114380.

Aspandiar, M.F., and Eggleton, R.A. (2002) Weathering of chlorite: I. Reactions and products in microsystems controlled by the primary mineral. Clays and Clay Minerals, 50, 685-698.

552 Bakker, E., Lanson, B., Findling, N., Wander, M.M., and Hubert, F. (2019)
553 Mineralogical differences in a temperate cultivated soil arising from different
554 agronomic processes and plant K-uptake. Geoderma, 347, 210-219.

555 Banfield, J.F., and Murakami, T. (1998) Atomic-resolution transmission electron
556 microscope evidence for the mechanism by which chlorite weathers to 1:1
557 semi-regular chlorite-vermiculite. American Mineralogist, 83, 348-357.

558 Brigatti, M.F., and Poppi, L. (1984) Crystal chemistry of corrensite; a review. Clays
559 and Clay Minerals, 32, 391-399.

560 Churchman, G.J. (2018) Game changer in soil science. Functional role of clay
561 minerals in soil. Journal of Plant Nutrition and Soil Science, 181, 99-103.

562 Churchman, G.J., and Lowe, D.J. (2012) Alteration, formation, and occurrence of
563 minerals in soils. In: Huang, P.M., Li, Y., and Summer, M.E. (eds.) Handbook of
564 Soil Sciences, 2nd ed., Vol. 1: Properties and Processes. CRC Press, Boca Raton,
565 Florida, pp. 20.1-20.72.

566 Compton, J.S., White, R.A., and Smith, M. (2003) Rare earth element behavior in
567 soils and salt pan sediments of a semi-arid granitic terrain in the Western Cape,
568 South Africa. Chemical Geology, 201, 239-255.

569 Cuadros, J. (2017) Clay minerals interaction with microorganisms: a review. Clay
570 Minerals, 52, 235-261.

571 Drits, V.A., Ivanovskaya, T.A., Sakharov, B.A., Zviagina, B.B., Gor'Kova, N.V.,

572 Pokrovskaya, E.V., and Savichev, A.T. (2011) Mixed-layer corrensite-chlorites
573 and their formation mechanism in the glauconitic sandstone-clayey rocks
574 (Riphean, Anabar Uplift). Lithology and Mineral Resources, 46, 566-593.

575 Egli, M., and Mirabella, A. (2021) The origin and formation of clay minerals in
576 Alpine soils. In: Hunt, A., Egli, M. and Faybishenko, B. (eds.). Hydrogeology,
577 Chemical Weathering, and Soil Formation, Chap. 6, pp. 121-137.

578 Egli, M., Mirabella, A., and Fitze, P. (2001) Clay mineral formation in soils of two
579 different chronosequences in the Swiss Alps. Geoderma, 104, 145-175.

580 Egli, M., Mirabella, A., and Fitze, P. (2003) Formation rates of smectites derived from
581 two Holocene chronosequences in the Swiss Alps. Geoderma, 117, 81-98.

582 Ehlmann, B.L., Mustard, J.F., Swayze, G.A., Clark, R.N., Bishop, J.L., Poulet, F., Des
583 Marais, D.J., Roach, L.H., Milliken, R.E., Wray, J.J., Barnouin-Jha, O., and
584 Murchie, S.L. (2009) Identification of hydrated silicate minerals on Mars using
585 MRO-CRISM: Geologic context near Nili Fossae and implications for aqueous
586 alteration. Journal of Geophysical Research, 37, L16202.

587 Fang, Q., Hong, H., Algeo, T.J., Huang, X., Sun, A., Churchman, G.J., Chorover, J.,
588 Chen, S., and Liu, Y. (2019) Microtopography-mediated hydrologic environment
589 controls elemental migration and mineral weathering in subalpine surface soils of
590 subtropical monsoonal China. Geoderma, 344, 82-98.

591 Feng, L., Chu, X., Zhang, T., and Huang, J. (2006) Liantuo sandstone: sedimentary

592 records under cold climate before the Nanhua big glaciations. Acta Petrologica
593 Sinica, 22, 2387-2393 (in Chinese with English abstract).

594 Gong, H., Zhang, R., Yue, L., Zhang, Y., and Li, J. (2015) Magnetic fabric from Red
595 clay sediments in the Chinese Loess Plateau. Scientific Reports, 5, 9701-9706.

596 Hazen, R.M., Sverjensky, D.A., Azzolini, D., Bish, D.L., Elmore, S.C., Hinnov, L.,
597 and Milliken, R.E. (2013) Clay mineral evolution. American Mineralogist, 98,
598 2007-2029.

599 He, H., Ji, S., Tao, Q., Zhu, J., Chen, T., Liang, X., Li, Z., and Dong, H. (2017)
600 Transformation of halloysite and kaolinite into beidellite under hydrothermal
601 condition. American Mineralogist, 102, 997-1005.

602 Hemingway, J.D., Rothman, D.H., Grant, K.E., Rosengard, S.Z., Eglinton, T.I., Derry,
603 L.A. and Galy, V.V. (2019) Mineral protection regulates long-term global
604 preservation of natural organic carbon. Nature, 570(7760), 228-231.

605 Hersbach, H., Bell, B., Berrisford, P., Biavati, G., Horányi, A., Muñoz Sabater, J.,
606 Nicolas, J., Peubey, C., Radu, R., Rozum, I., Schepers, D., Simmons, A., Soci, C.,
607 Dee, D., and Thépaut, J-N. (2019) ERA5 monthly averaged data on single levels
608 from 1979 to present. Copernicus Climate Change Service (C3S) Climate Data
609 Store (CDS), DOI: 10.24381/cds.f17050d7.

610 Hong, H., Churchman, G.J., Gu, Y., Yin, K., and Wang, C. (2012) Kaolinite-smectite
611 mixed-layer clays in the Jiujiang red soils and their climate significance.

612 Geoderma, 173, 75-83.

613 Hong, H., Churchman, G.J., Yin, K., Li, R., and Li, Z. (2014) Randomly interstratified
614 illite-vermiculite from weathering of illite in red earth sediments in Xuancheng,
615 southeastern China. Geoderma, 214-215, 42-49.

616 Hong, H., Cheng, F., Yin, K., Churchman, G.J., and Wang, C. (2015)
617 Three-component mixed-layer illite/smectite/kaolinite (I/S/K) minerals in
618 hydromorphic soils, south China. American Mineralogist, 100, 1883-1891.

619 Hu, X., Huang, C., Mei, H., and Zhang, H. (2021) Landslide susceptibility mapping
620 using an ensemble model of Bagging scheme and random subspace–based naïve
621 Bayes tree in Zigui County of the Three Gorges Reservoir Area, China. Bulletin
622 of Engineering Geology and the Environment, 80, 5315-5329.

623 Hubei Province Geological Survey (1965) Geological Map of Badong (1:200,000).

624 Kleber, M., Bourg, I.C., Coward, E.K., Hansel, C.M., Myneni, S.C.B., and Nunan, N.
625 (2021) Dynamic interactions at the mineral–organic matter interface. Nature
626 Reviews Earth & Environment, 2, 402-21.

627 Kogure, T. (2020) Visualization of clay minerals at the atomic scale. Clay Minerals,
628 55, 203-218.

629 Kogure, T., and Inoue, A. (2005) Determination of defect structures in kaolin minerals
630 by high-resolution transmission electron microscopy (HRTEM). American
631 Mineralogist, 90, 85-89.

632 Kogure, T., Drits, V.A., and Inoue, S. (2013) Structure of mixed-layer
633 corrensite-chlorite revealed by high-resolution transmission electron microcopy
634 (HRTEM). American Mineralogist, 98, 1253-1260.

635 Korchagin, J., Bortoluzzi, E.C., Moterle, D.F., Petry, C., and Caner, L. (2019)
636 Evidences of soil geochemistry and mineralogy changes caused by eucalyptus
637 rhizosphere. Catena, 175, 132-143.

638 Li, S., He, H., Tao, Q., Zhu, J., Tan, W., Ji, S., Yang, Y., and Zhang, C. (2020)
639 Kaolinization of 2:1 type clay minerals with different swelling properties.
640 American Mineralogist, 105, 687-696.

641 Liu, D., Tian, Q., Yuan, P., Du, P., Zhou, J., Li, Y., Bu, H., and Zhou, J. (2019) Facile
642 sample preparation method allowing TEM characterization of the stacking
643 structures and interlayer spaces of clay minerals. Applied Clay Science, 171, 1-5.

644 McLennan, S.M. (2001) Relationships between the trace element composition of
645 sedimentary rocks and upper continental crust. Geochemistry, Geophysics,
646 Geosystems, 2, 2000GC000109.

647 Moore, D.M., Reynolds, R.C., Jr. (1989) X-ray Diffraction and the Identification and
648 Analysis of Clay Minerals. Oxford University Press, New York, 332 pp.

649 Nakao, A., Sugihara, S., Maejima, Y., Tsukada, H., and Funakawa, S. (2017)
650 Ferralsols in the Cameroon plateaus, with a focus on the mineralogical control on
651 their cation exchange capacities. Geoderma, 285, 206-216.

National Earth System Science Data Center, National Science & Technology Infrastructure of China (2000) (http://www.geodata.cn).

Norrish, K. (1973) Factors in the weathering of mica to vermiculite. Proceedings of 1972 International Clay Conference, Madrid (J. M. Serratosa, editor). CSIC, Madrid, pp. 417-432.

Righi, D., Huber, K., and Keller, C. (1999) Clay formation and podzol development from postglacial moraines in Switzerland. Clay Minerals, 34, 319-332.

Ryan, P.C., and Huertas, F.J. (2009) The temporal evolution of pedogenic Fe–smectite to Fe–kaolin via interstratified kaolin–smectite in a moist tropical soil chronosequence. Geoderma, 151, 1-15.

Schroeder, P.A. (2018). Clays in the Critical Zone. Cambridge University Press, Online ISBN: 9781316480083, 252 pp.

Shi, X.Z., Yu, D.S., Warner, E.D., Pan, X.Z., Petersen, G.W., Gong, Z.G., and Weindorf, D.C. (2004) Soil database of 1: 1,000,000 digital soil survey and reference system of the Chinese genetic soil classification system. Soil Survey Horizons, 45, 129-136.

Soil Survey Staff (2014) Keys to Soil Taxonomy, 12th Ed., USDA. National Resources Conservation Service, National Soil Survey Center, Lincoln, Nebraska, 338 pp.

Sugimori, H., Iwatsuki, T., and Murakami, T. (2008) Chlorite and biotite weathering,

672 Fe2+-rich corrensite formation, and Fe behavior under low PO2 conditions and
673 their implication for Precambrian weathering. American Mineralogist, 93,
674 1080-1089.

675 Vázquez-Ortega, A., Perdrial, J., Harpold, A., Zapata-Ríos, X., Rasmussen, C.,
676 McIntosh, J., Schaap, M., Pelletier, J.D., Brooks, P.D., Amistadi, M.K., and
677 Chorover, J. (2015) Rare earth elements as reactive tracers of biogeochemical
678 weathering in forested rhyolitic terrain. Chemical Geology, 391, 19-32.

679 Velde, B., Meunier, A. (2008) The origin of clay minerals in soils and weathered rocks.
680 Springer, Berlin-Heidelberg, 406 pp.

681 Wang, G., Wang, H., Wen, J. (2019) Identification of interstratified mica and
682 pyrophyllite monolayers within chlorite using advanced scanning/transmission
683 electron microscopy. American Mineralogist, 104, 1436-1443.

684 Wang, Y. (2008) Study on the Farmland Soil Geochemical Characteristics of Tongzi
685 town in Jiangan County, Yibin, China. Master's thesis, Chengdu University of
686 Technology, Chengdu, Sichuan Province.

687 Watanabe, T., Hasenaka, Y., Hartono, A., Sabiham, S., Nakao, A., and Funakawa, S.
688 (2017) Parent materials and climate control secondary mineral distributions in
689 soils of Kalimantan, Indonesia. Soil Science Society of America Journal, 81,
690 124-137.

691 Weil, R.R., and Brady, N.C. (2017) The Nature and Properties of Soils, 15th Ed.,

692 Prentice-Hall Press, New York, 1104 pp.

693 Wilson, M.J. (1999) The origin and formation of clay minerals in soils: past, present
694 and future perspectives. Clay Minerals, 34, 7-25.

695 Wilson, M.J. (2004) Weathering of the primary rock-forming minerals: processes,
696 products and rates. Clay Minerals, 39, 233-266.

697 Yan, R., Zhou, H., Zeng, W., Jiang, L., Zhou, Z., and Chen, T. (2006) Geochemical
698 characteristics of Khondalite Series within Kongling Group in Yichang City,
699 Hubei Province. Geological Science and Technology Information, 25, 41-46 (in
700 Chinese with English abstract).

701 Yousefifard, M., Ayoubi, S., Poch, R.M., Jalalian, A., Khademi, H., and Khormali, F.
702 (2015) Clay transformation and pedogenic calcite formation on a lithosequence
703 of igneous rocks in northwestern Iran. Catena, 133, 186-197.

704 Zhang, M., Peng, S., Zhang, L., Fang, J., Zhang, X., and Han, Q. (2016) New
705 recognition of carbonate nodules genesis in Sinian Doushantuo Formation in
706 Zigui Area and its geological implication. Earth Science, 41, 1977-1994 (in
707 Chinese with English abstract).

708

This is the peer-reviewed, final accepted version for American Mineralogist, published by the Mineralogical Society of America.
The published version is subject to change. Cite as Authors (Year) Title. American Mineralogist, in press.
DOI: https://doi.org/10.2138/am-2022-8740. http://www.minsocam.org/

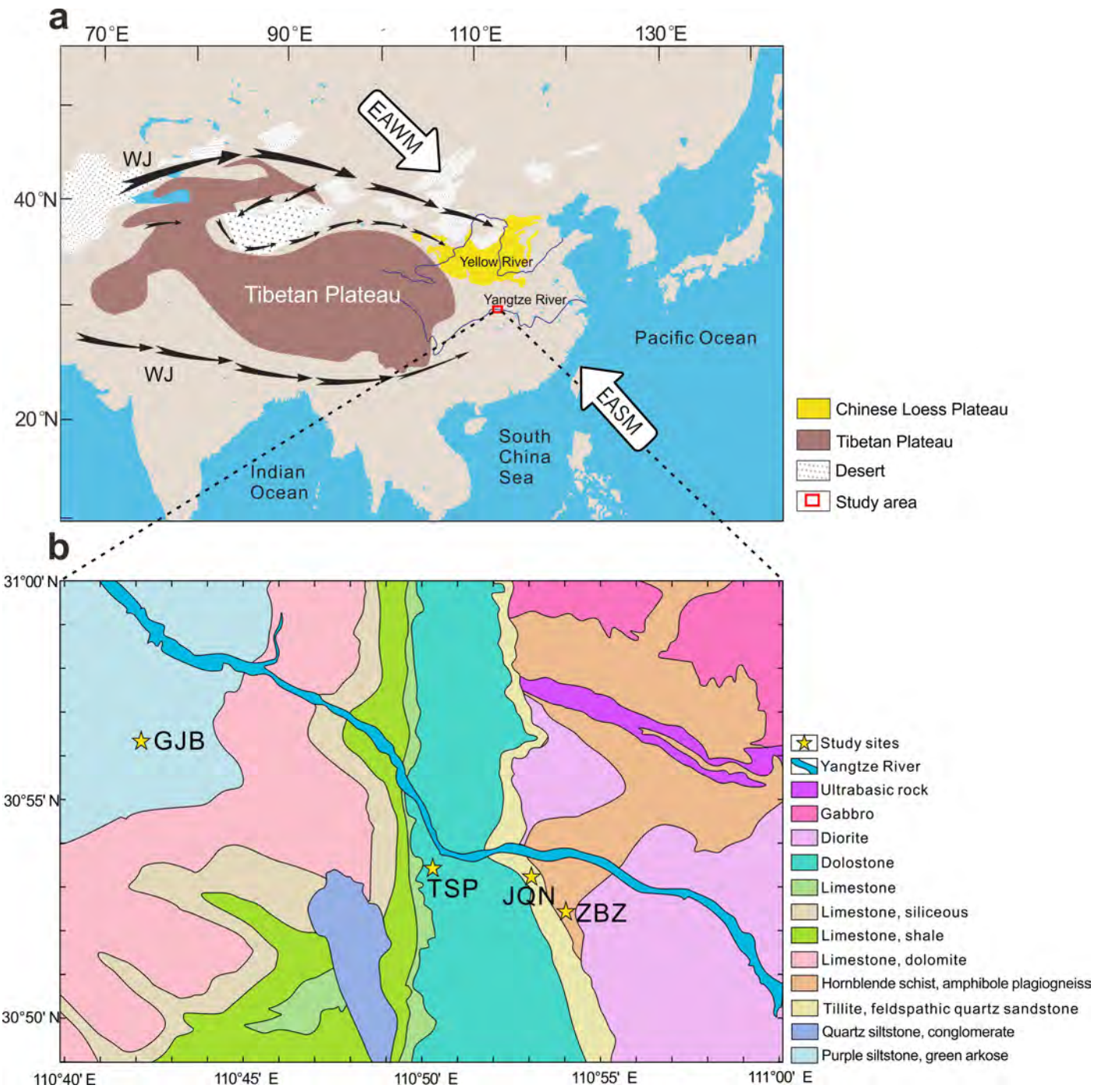

Fig. 1. Maps of location and geologic setting of the Zigui study area. (a) East and central Asia, showing study area on the middle reaches of the Yangtze River, southern China, which is influenced by the East Asian summer monsoon (EASM) and East Asian winter monsoon (EAWM) (modified from Gong et al., 2015). (b) Locations of four study soils and bedrock lithologies in the Zigui study area. Abbreviations: WJ = Westerly Jet; GJB = Gejiabei; TSP = Taishangping; JQN = Jiuqunao; and ZBZ = Zhongbazi.

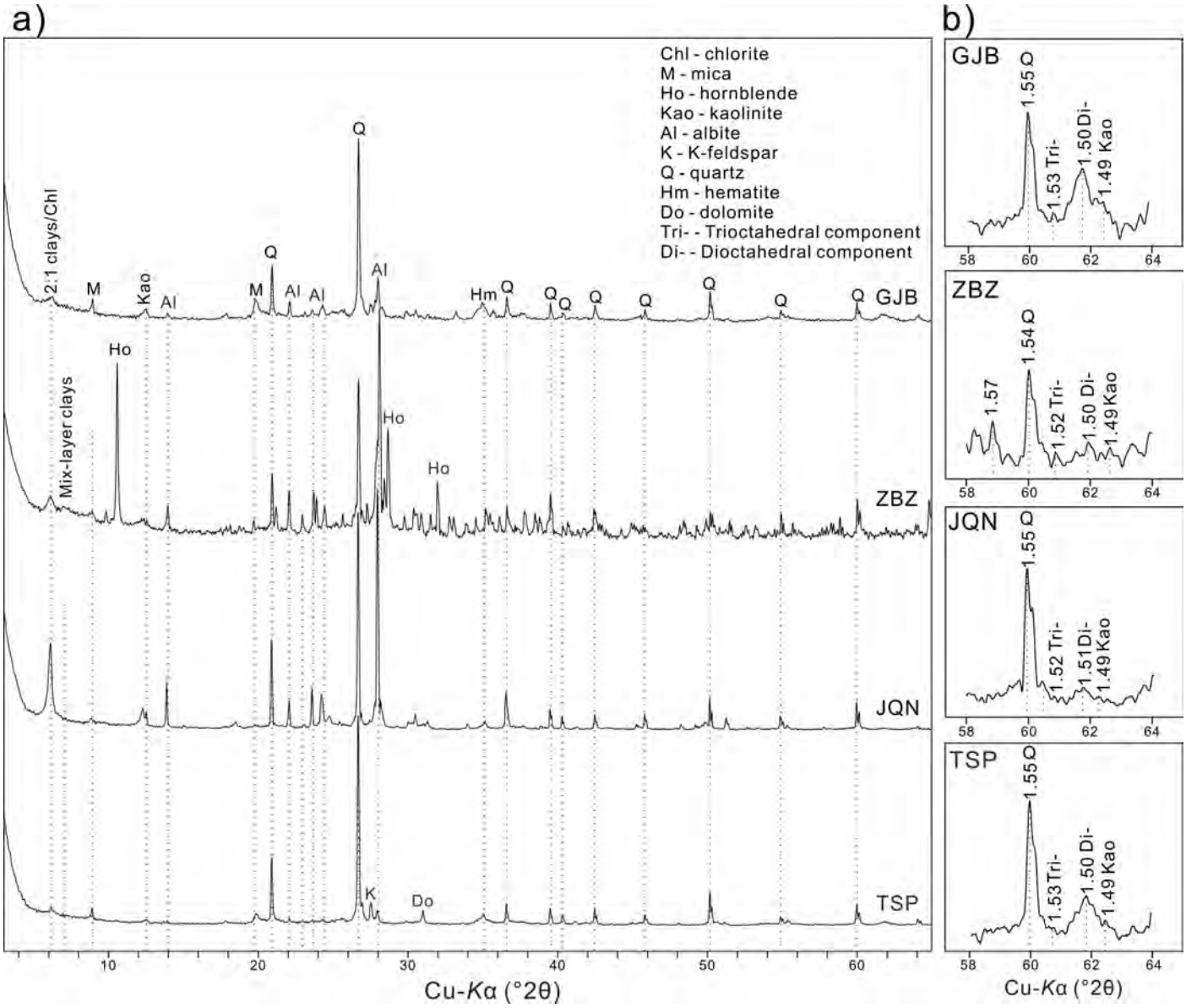

Fig. 2. Representative XRD patterns for each study soil: (a) randomly-oriented powder mounts, and (b) *d*(060) region. See legend in Figure 3 for peak identifier abbreviations.

This is the peer-reviewed, final accepted version for American Mineralogist, published by the Mineralogical Society of America.
The published version is subject to change. Cite as Authors (Year) Title. American Mineralogist, in press.
DOI: https://doi.org/10.2138/am-2022-8740. http://www.minsocam.org/

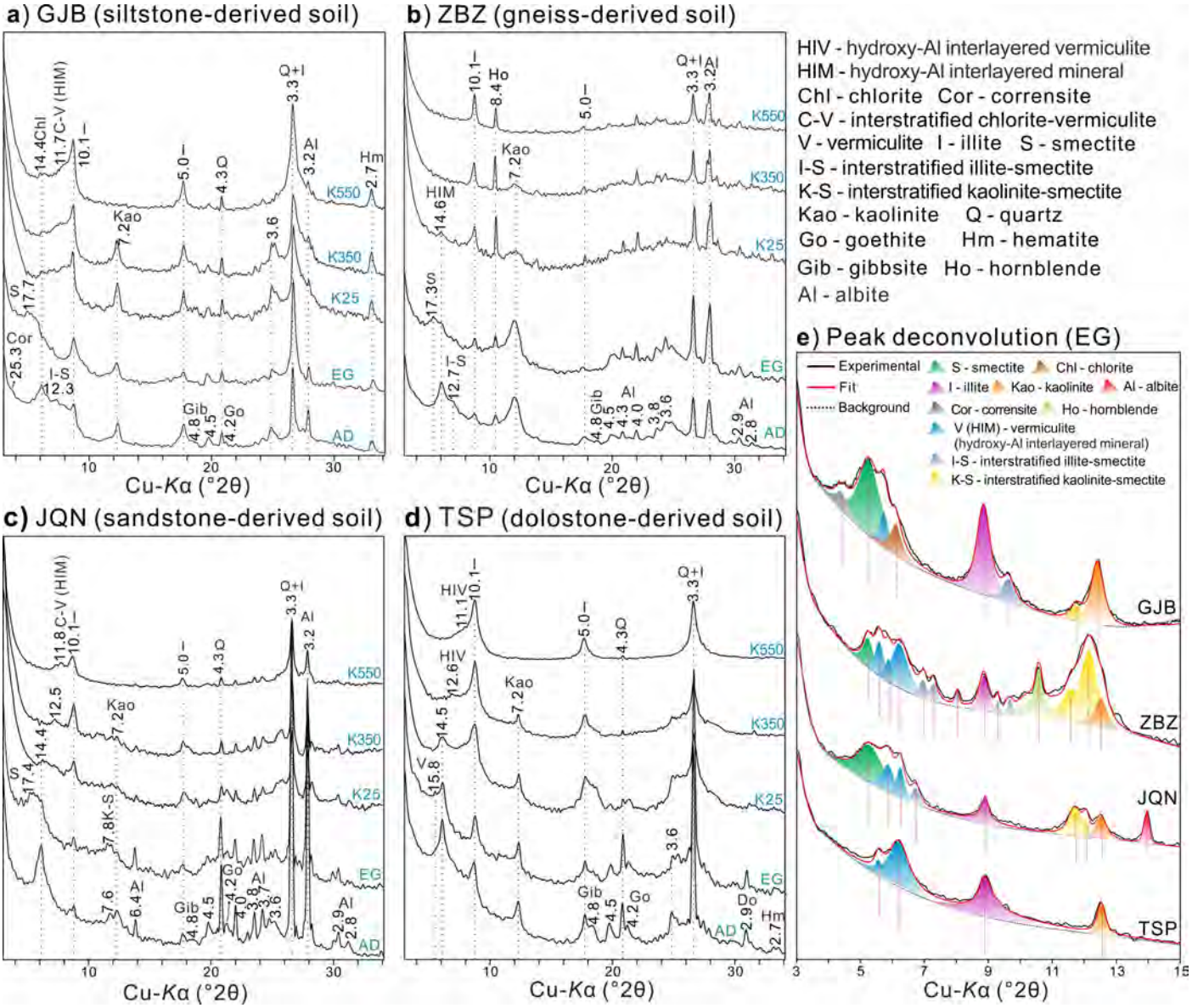

Fig. 3. XRD patterns of representative soil samples from B horizons of four study soils: (a) GJB, (b) ZBZ, (c) JQN, and (d) TSP. (e) Deconvolutions of XRD peaks in the 3-15 °2θ region. AD = Air-dried treatment; EG = ethylene glycol solvation; K25, K350, K550 = K-saturation at room temperature and after heat treatments at 350 and 550 °C.

This is the peer-reviewed, final accepted version for American Mineralogist, published by the Mineralogical Society of America.
The published version is subject to change. Cite as Authors (Year) Title. American Mineralogist, in press.
DOI: https://doi.org/10.2138/am-2022-8740. http://www.minsocam.org/

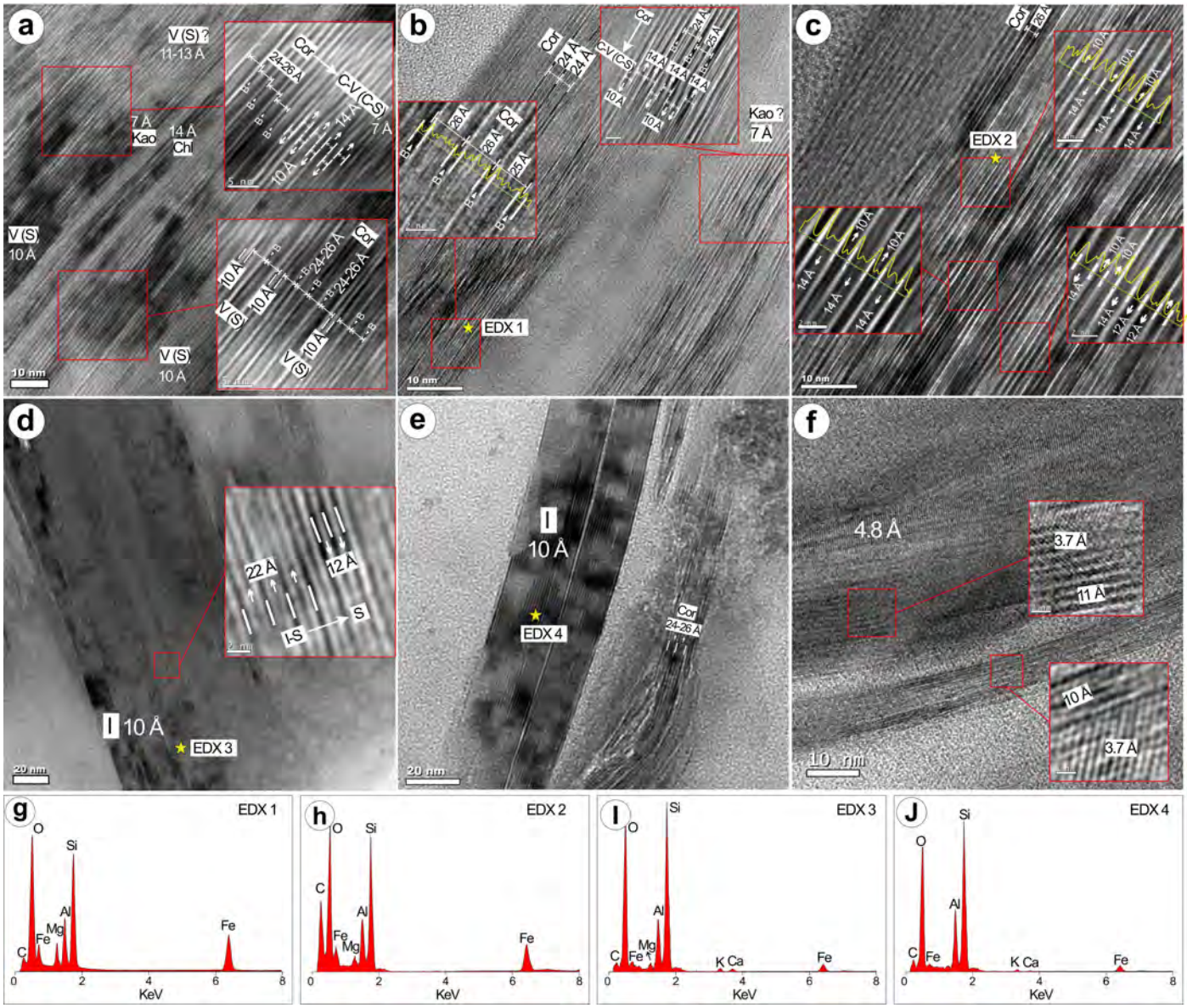

Fig. 4. HRTEM images of the GTB soil sample. (a-c) Lattice-fringe images showing packets of corrensite layers (24-26 Å spacing) and regular/random chlorite (~14 Å) and vermiculite (collapsed as ~10 Å) layers. (d) Lattice-fringe image showing possible alteration of mixed-layer illite and smectite layers (~22 Å) to smectite-group minerals (~12 Å). (e) TEM image of a straight illite layer and a curved corrensite-like layer. (f) Gibbsite (4.8 Å) and goethite grains (3.7 Å) within 10-11 Å clay packets. (g-j) EDX spectra of the clay fringes.

This is the peer-reviewed, final accepted version for American Mineralogist, published by the Mineralogical Society of America.
The published version is subject to change. Cite as Authors (Year) Title. American Mineralogist, in press.
DOI: https://doi.org/10.2138/am-2022-8740. http://www.minsocam.org/

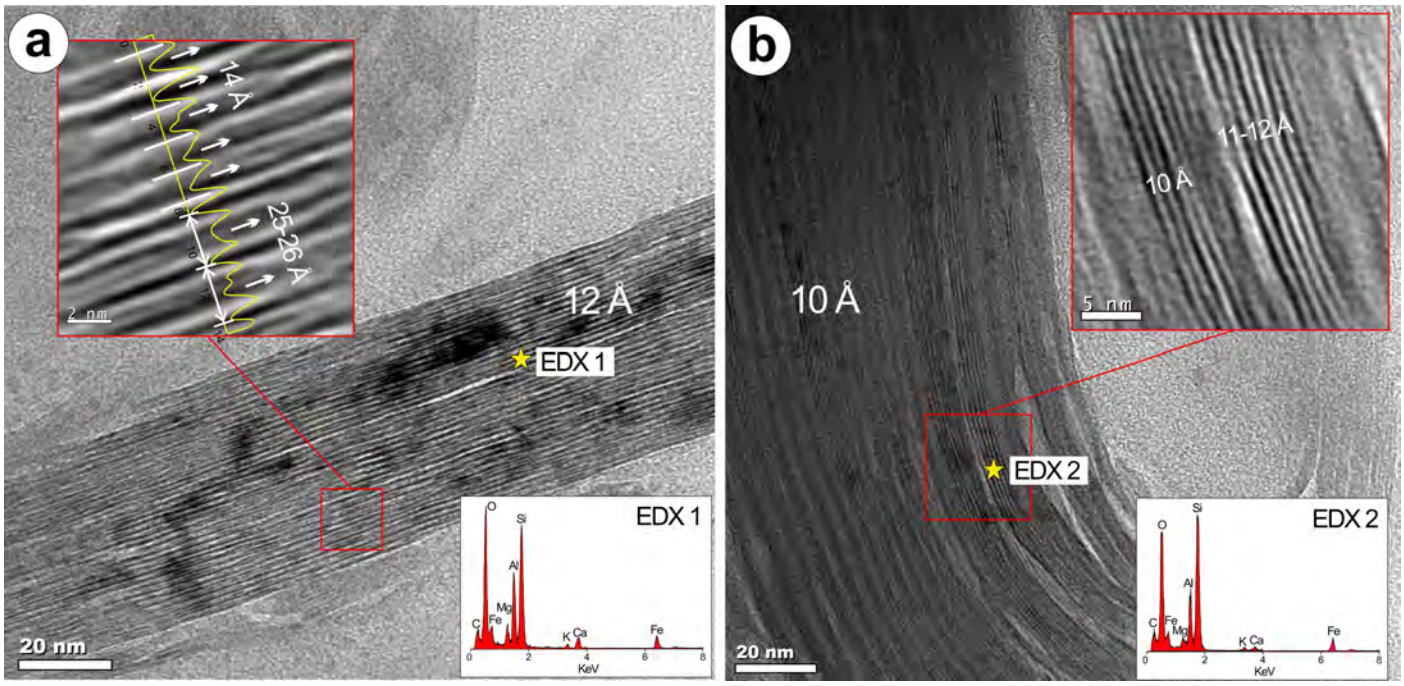

Fig. 5. HRTEM images of the ZBZ soil sample. (a) Lattice-fringe images showing packets of collapsed smectite layers (~12 Å), chlorite layers (14 Å), and corrensite-like layers (25 Å). (b) Curved clay fringes consisting of 10-12 Å layers, most likely an interstratified illite-smectite phase.

This is the peer-reviewed, final accepted version for American Mineralogist, published by the Mineralogical Society of America.
The published version is subject to change. Cite as Authors (Year) Title. American Mineralogist, in press.
DOI: https://doi.org/10.2138/am-2022-8740. http://www.minsocam.org/

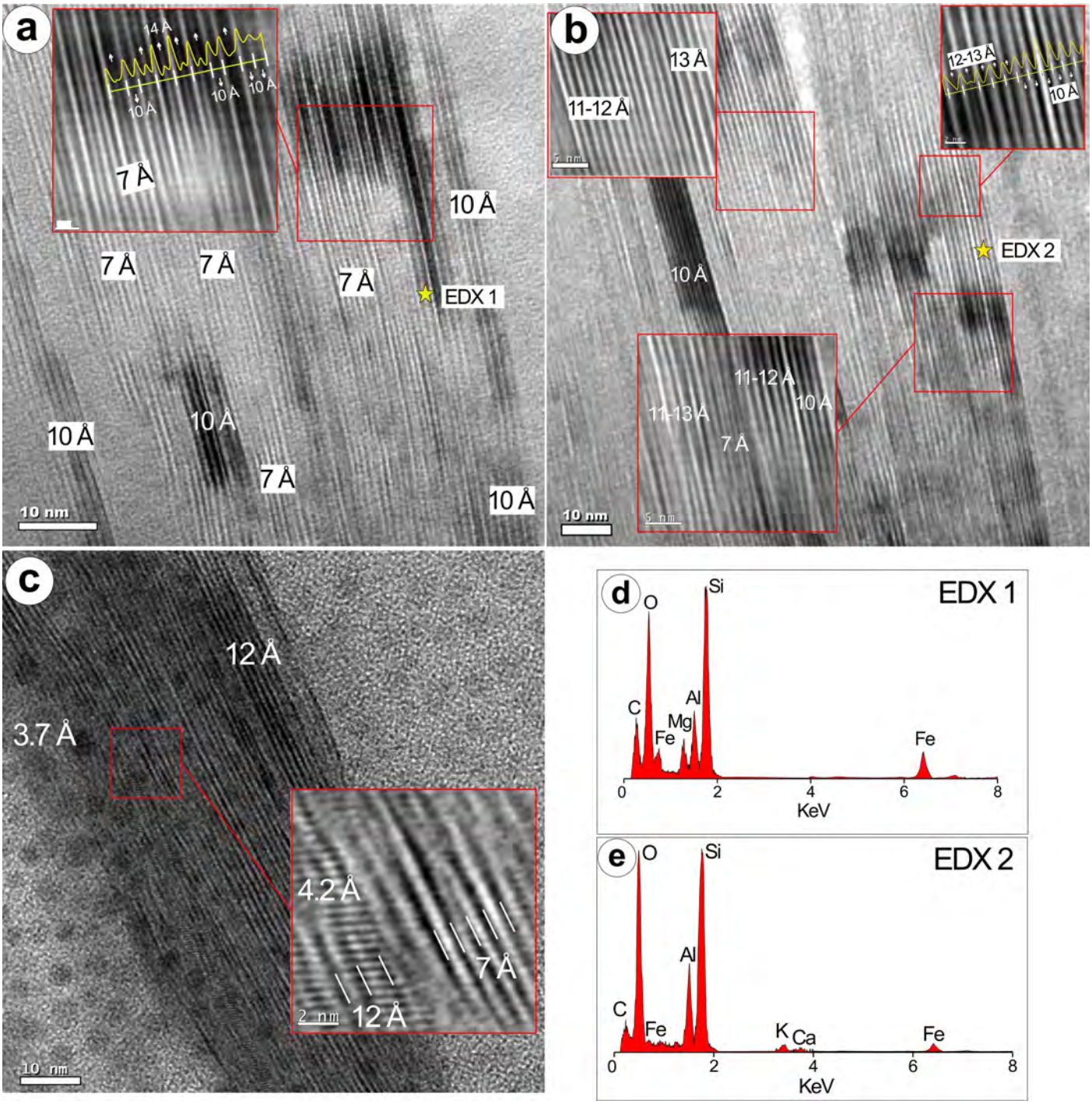

Fig. 6. HRTEM images of the JQN soil sample. (a-b) Crystals with complex microstructures show layers with spacings of 7-14 Å. (c) Hematite (3.7 Å) and goethite (4.2 Å) grains within adjacent 12-Å and 7-Å clay packets. (d-e) EDX spectra of the clay fringes.

This is the peer-reviewed, final accepted version for American Mineralogist, published by the Mineralogical Society of America.
The published version is subject to change. Cite as Authors (Year) Title. American Mineralogist, in press.
DOI: https://doi.org/10.2138/am-2022-8740. http://www.minsocam.org/

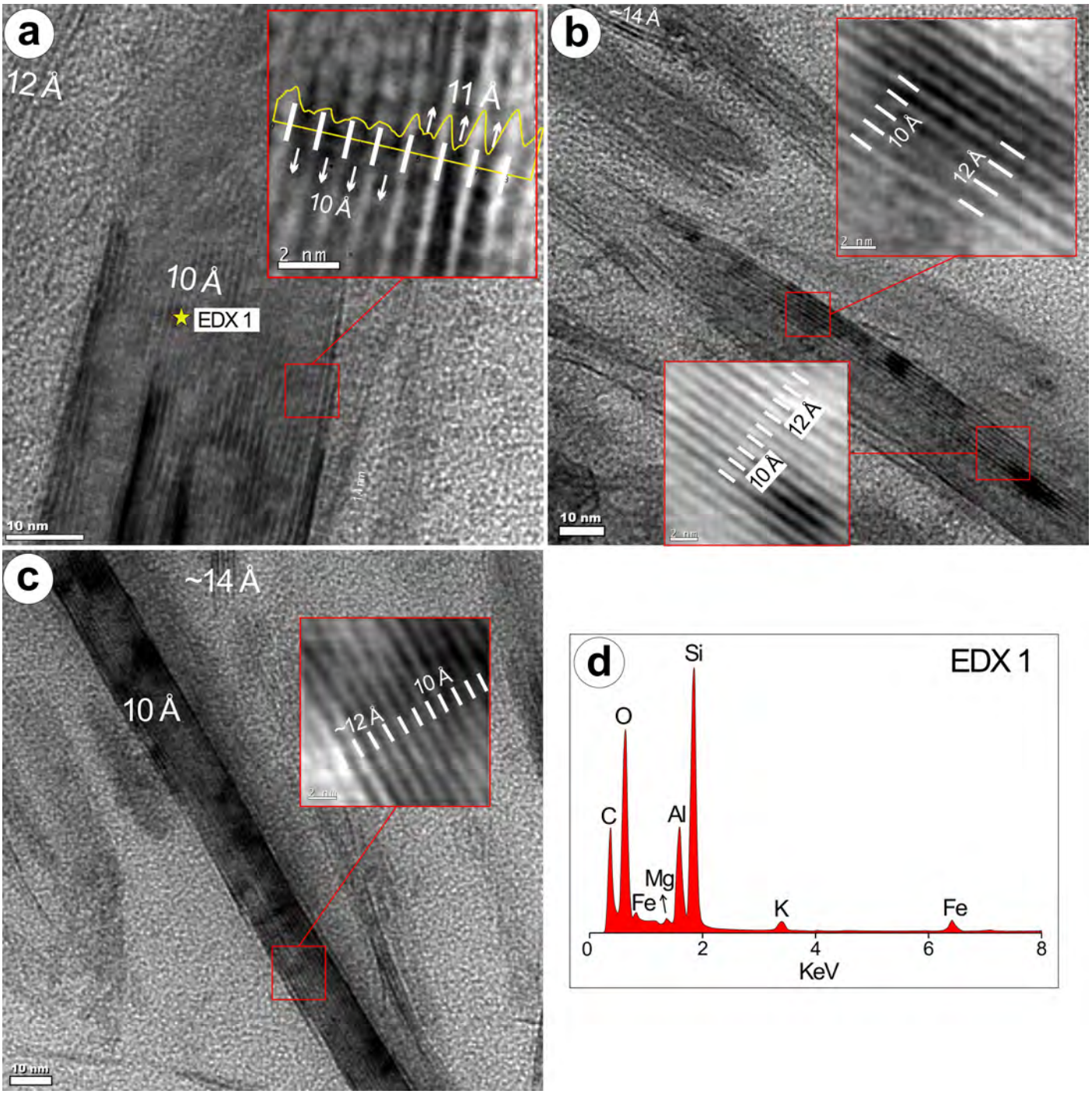

Fig. 7. HRTEM images of the TSP soil sample. (a-c) Lattice-fringe images showing alteration of illite at edge layers. Some discrete 14-Å layers are also present, consistent with the presence of HIV. (d) EDX spectra of the illite layers.

This is the peer-reviewed, final accepted version for American Mineralogist, published by the Mineralogical Society of America.
The published version is subject to change. Cite as Authors (Year) Title. American Mineralogist, in press.
DOI: https://doi.org/10.2138/am-2022-8740. http://www.minsocam.org/

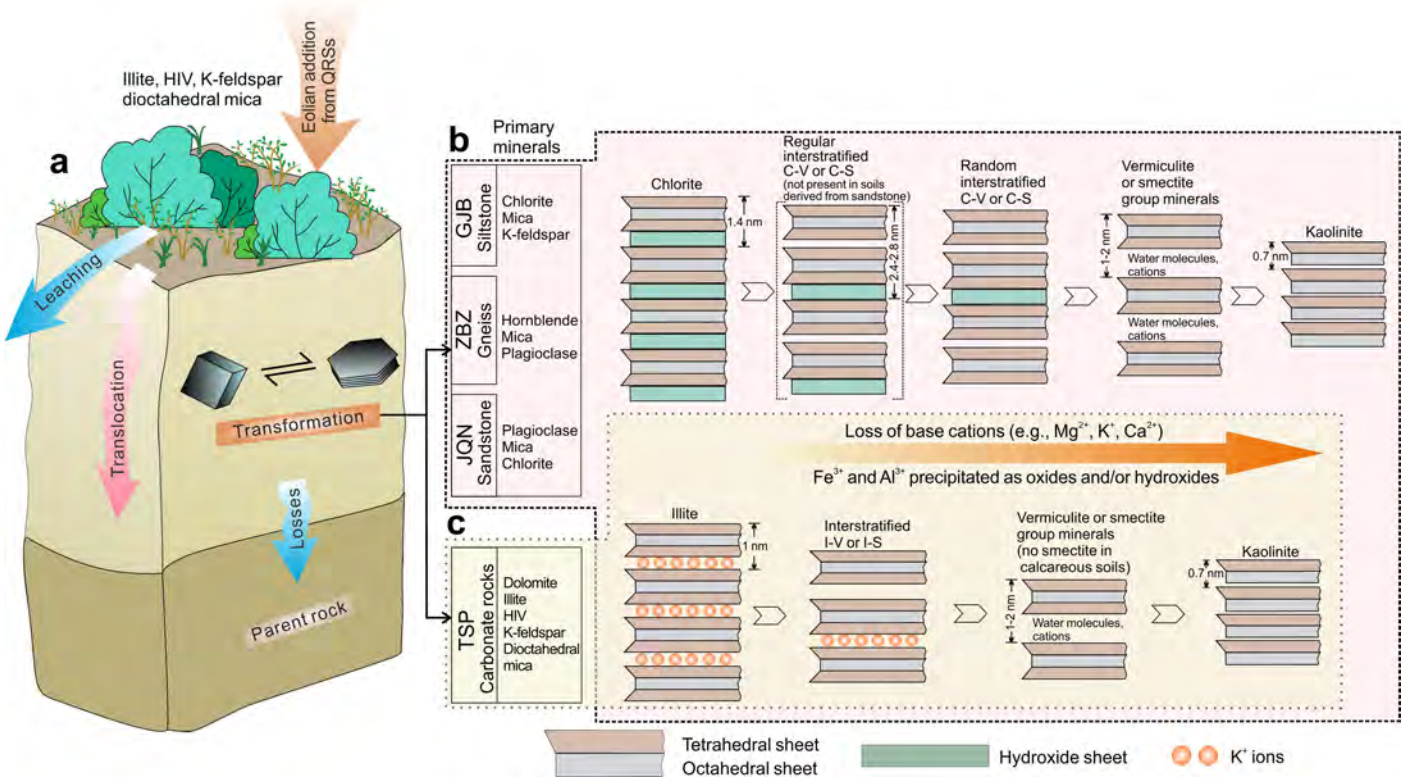

Fig. 8. Weathering and transformation pathways in the study soils. a) A schematic illustration of additions, losses, translocations, and transformations as the fundamental processes driving soil-profile development (modified after Weil and Brady, 2017). b) Main pathways for clay-mineral formation and alteration in soils derived from various parent rocks. QRS: Quaternary red soil; HIV: hydroxy-interlayered vermiculite.